Biomedical Materials

PAPER • **OPEN ACCESS**

Three-dimensionally two-photon lithography realized vascular grafts

To cite this article: T Limongi *et al* 2021 *Biomed. Mater.* **16** 035013

Biomedical Materials

CrossMark

OPEN ACCESS

RECEIVED
30 October 2020

ACCEPTED FOR PUBLICATION
13 November 2020

PUBLISHED
1 March 2021

PAPER

Three-dimensionally two-photon lithography realized vascular grafts

T Limongi[1,2], L Brigo[2,3], L Tirinato[4], F Pagliari[4], A Gandin[3,5], P Contessotto[3], A Giugni[6] and G Brusatin[3,5]

[1] Politecnico di Torino, Department of Applied Science and Technology, Torino 10129, Italy
[2] Equal contribution.
[3] University of Padova, Department of Industrial Engineering, via Marzolo 9, Padova 35131, Italy
[4] German Cancer Research Center (DKFZ), Division of BioMedical Physics in Radiation Oncology, Heidelberg 69120, Germany
[5] University of Padova and INSTM, Department of Molecular Medicine, via Ugo Bassi 58/B, Padova 35131, Italy
[6] King Abdullah University of Science and Technology (KAUST), Physical Sciences and Engineering Division, Thuwal 23955-6900, Saudi Arabia

E-mail: giovanna.brusatin@unipd.it and andrea.giugni@kaust.edu.sa

Keywords: microstructured scaffolds, 3D fabrication, two-photon laser lithography, endothelial cells, vascular tissue engineering

Abstract

Generation of artificial vascular grafts as blood vessel substitutes is a primary challenge in biomaterial and tissue-engineering research. Ideally, these grafts should be able to recapitulate physiological and mechanical properties of natural vessels and guide the assembly of an endothelial cell lining to ensure hemo-compatibility. In this paper, we advance on this challenging task by designing and fabricating 3D vessel analogues by two-photon laser lithography using a synthetic photoresist. These scaffolds guarantee human endothelial cell adhesion and proliferation, and proper elastic behavior to withstand the pressure exerted by blood flow.

1. Introduction

Blood vessel damage is recognized as main cardiovascular health problem [1–4]. Even though autologous veins and arteries transplantation represents the election treatment for stent insertion and angioplasty, autologous materials are not always available in the case of trauma, vessel diseases or surgery. Tissue-engineered vascular graft (TEVG) represents an efficient alternative for the resolution of blood vessel ruptures or other deficiencies. These scaffolds may offer biomimetic support for three-dimensional (3D) tissue restoration of large heart veins, arteries and capillaries [5–12].

To allow integration in a vascular network, the design and fabrication of TEVGs has to satisfy specific physical, mechanical, and biological benchmarks, and do this safely over the expected lifetime of the implant [13]. At the macroscopic scale, the engineered vessel has to maintain its shape and elastic property, withstanding the pressure exerted by the blood flow, preventing permanent bulging that lead to aneurysm or rupture. It also has to self-maintain its shape against external stimuli and stresses, avoiding permanent crushes or bottleneck occlusions. These constraints pose range-limits to the TEVG design, its elastic/plastic characteristic as well as on the homogeneity and tolerances.

Of paramount importance, the exposed vessel surface has to be fully bio- and hemo-compatible, to prevent thrombi formation and warranting minimal alteration in the blood flow and pressure drop along the graft. These synthetic or natural bio-ink should be 3D printed in TEVGs to create linear or branched hollow structures, or other complex scaffold shapes. Such vascular grafts should be the populated with cells *ex vivo*, by culturing patient-specific, autologous cells directly on the scaffolds before implantation [14–16].

Microscale engineering allows determine the desired elastic and torsional responses in all the three dimensions, allowing to adapt the physical response by appropriate design of the scaffold texture. For this, 3D fabrication techniques are rapidly expanding in the field of scaffold development for *in vitro* cell-culture and tissue-engineering applications, in particular two-photon laser lithography (2PLL). By 2PLL a photosensitive material, that is typically in a liquid state, is polymerized in 3D at the micro- and mesoscale, allowing high surface-to-volume ratio and

interconnected porous network. This nanofabrication has been recently used in a wide range of tissue-engineering applications allowing the fabrication of scaffolds designed with micro- and nano-sized structures [17–22]. Intriguingly, such deterministic bottom-up approach to graft realization also allows the mold-and-replica fabrication on a large scale.

In this paper, we used 2PLL for the 3D fabrication of vessel analogues, designed after computer simulation for optimal physical properties. A biocompatible resin allowing 2PLL fabrication was used for the realization of the microstructures of honeywell geometry, that we show could be populated by endothelial cells generating a homogeneous and continuous cell lining. In so doing, we challenged ourself on an unmet medical need, that is the generation of small size vessel diameters (diameter of about 100 μm), whose fabrication currently escapes conventional methodologies [17, 23–27]. The resulting structure guided human umbilical vein endothelial cells (HUVECs) adhesion and proliferation providing proof-of-principle of effective cell repopulation.

2. Materials and methods

2.1. Structure design and mechanical properties simulations

The mechanical response to external stresses applied to the scaffold's sidewall structure was simulated using finite element analysis (FEA) of the elastic equilibrium condition, accomplished with the elastic analysis module of the CAD software. The elastic reaction of the structure was evaluated variating the geometric parameters of the honeycomb structure (d_1, d_2, d_3, indicated in figure 1) in response to a set of specific applied stresses, taking into account the physical properties of the polymer used to fabricate the scaffolds. For this, we assigned to the whole structure the polymer physical constants at the temperature of 37 °C (cell-culture experiment temperature) interpolating reported literature data (IP-DIP commercial photoresist, Nanoscribe GmbH, density of solid 1.3 g cm^{-3} [28, 29], Young's modulus 2.10 GPa, Yield strength 67.2 MPa, Poisson's ratio: 0.49 [30], thermal length expansion coefficient of bulk 6×10^{-5} m^{-1} K^{-1} [31].

For the numerical calculation, we schematized the structure by a non-uniform adaptive mesh with a minimum of 241 905 nodes and 113 463 elements, with an average size = 0.2 of the single designed element. We targeted a stop criterion of 5% of the von Mises stress, i.e. the computation stopped when the difference between the last two refinement results was less than the specified value, aiming the convergence of the parameter. The von Mises stress, deriving from the deviatoric strain energy density, is a local metric of measurement that we use to determine the punctual structure yielding under the application of arbitrary global static load conditions. Thus, indicating an upper limit for the elasticity of the material, the von Mises criterion defines a quantity comparable with experimentally observable yielding sites, allowing to understand when the real sample is in the elastic regime or has bent permanently.

2.2. 3D scaffold fabrication and scanning electron microscopy (SEM) characterization

Tubular porous microstructures were fabricated by a commercially available 2PLL system (Photonic Professional GT, Nanoscribe GmbH) equipped with a femtosecond-pulsed laser at 780 nm. Using the dip-in laser writing mode, the laser is focused into a droplet of IP-DIP photoresist using a high numerical-aperture objective (NA = 1.4) and a 63× immersion microscope objective.

Arrays of cylindrical structures, presenting hexagonal pores arranged in a honeycomb lattice, of nominal 100 μm overall height and 5 μm wall thickness and depth, were fabricated on fused silica glass slides. Laser writing was performed with scan speeds in the range of 4–8 mm s^{-1} at laser powers from 15 mW to 25 mW. A circular crown (Øin = 80 μm; Øout = 110 μm; height = 5 μm) was also fabricated as a base layer for the tubular scaffolds to promote structure stable adhesion to the substrate. To remove the un-polymerized material, the sample was immersed for 30 min at room temperature in propylene glycol monomethyl ether acetate (PGMEA) and rinsed in isopropyl alcohol (IPA) for 5 min. A selection of scaffolds was successively sputter-coated with a 10 nm Au–Pd layer and inspected by scanning electron microscopy (SEM, Quanta 450, FEI, USA).

2.3. IP-DIP degradation

To test if IP-DIP can be modified by cell medium (DMEM, 1× Gibco, high glucose—Thermo Fisher Scientific (Cat n 41965-039) or PBS (PBS:1× D-PBS w/o Ca and Mg, Euroclone, Cat n ECM4004XL), sets of six samples with dimensions of approximately 2 × 2 × 1 mm^3 were prepared. A PDMS gasket with a hole in the middle was placed on the surface of a glass coverslip and filled with IP-Dip resist. Each sample was then polymerized using a led lamp (DELOLUX 20/400 nm) with peak emission at the wavelength of 400 nm, for 60 s using a power density of 500 mW cm^{-2}. The samples, after a quick wash-rinsing with ethanol, were mass characterized by three weightings, finally placed inside a 12 wells plate. Pictures were taken of each sample for visual comparison. Namely, samples 1, 2 and 3 were covered with 1.5 ml of cell medium, while for samples 4, 5 and 6, PBS was used instead. The pH of the solutions in each well was measured, then the multi-well was placed inside an incubator to keep the temperature stable at 37 °C.

Every 3 d the pH of medium or PBS of each well was checked and then replaced by a fresh solution. In the meantime, the samples were rinsed quickly with

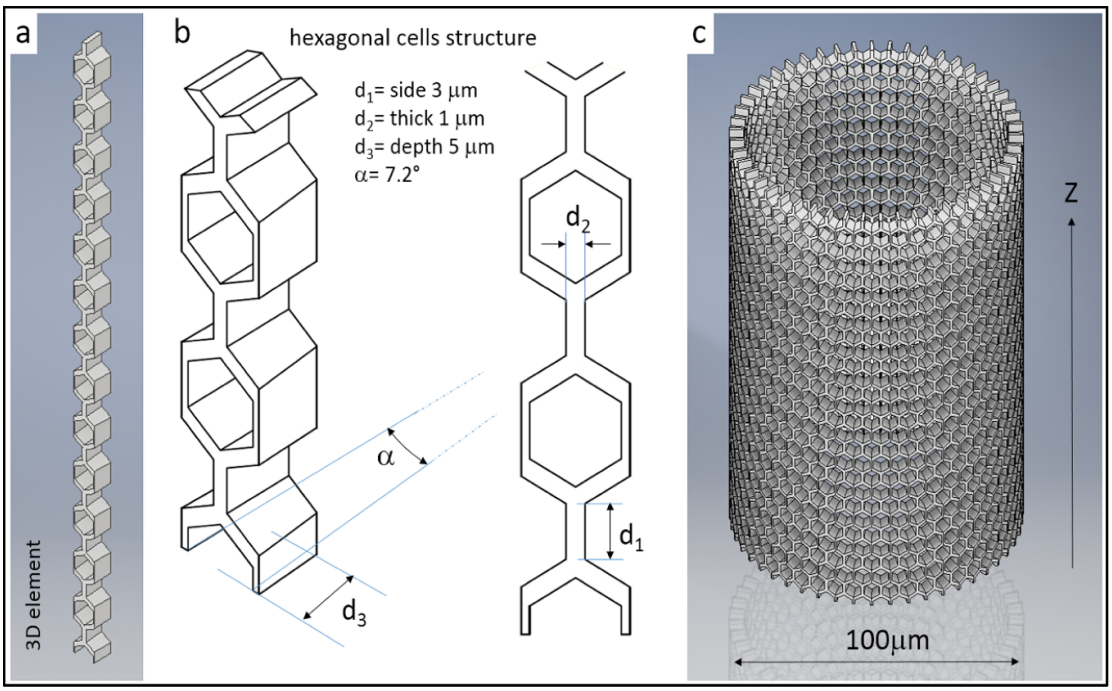

Figure 1. Scaffold structure design: skeletal construction elements used along with the indication of design parameters (a), (b), and 3D rendering (c) of the final cylindrical simulated hollow scaffold characterized by an ad hoc honeycomb wall structure designed considering the average size of the endothelial cells. The design parameters, hexagon side length, thickness and depth of the wall, along with the physical properties of the IP-DIP biocompatible polymer, all concur to determinate the overall 3D elastic properties of the scaffold.

pure ethanol, left on a lab paper to dry and then weighed. After 10 d, all samples did not show evidence of shape change nor weight loss.

2.4. Cell culture and scaffold seeding

HUVECs (ATCC®, PCS-100-010™) were cultured in Vascular Cell Basal Medium supplemented with Endothelial Cell Growth Kit–VEGF (ATCC PCS-100-041) according to the manufacturer's instructions, and with 10 units ml^{-1} penicillin and 10 µg ml^{-1} streptomycin. Cells were grown at 37 °C in a 5% CO_2 humidified atmosphere until reaching the subconfluence. Then, cells were detached using 1× Tryple™ Express Enzyme (Cat. Number 12604013; Thermo Fisher Scientific), and the reaction was stopped with a complete medium. After centrifugation for 5 min at 1000 RPM, the pellet was resuspended in fresh complete medium. A Neubauer chamber was used to count the cells.

Scaffolds were placed in a 12 well plate (Cat. Number 351143; Corning Life Sciences), sterilized by fast immersion in ethanol 99.8% (Sigma-Aldrich; CAS Number: 64-17-5) washed twice in sterile water, dried in a laminar flow hood and further sterilized by UV irradiation for 2 h. Substrates were immersed in a complete medium for 3 d in a cell-culture incubator (37 °C, 5% CO_2, 95% humidity), to provide a protein deposition on the scaffold surface. Before plating the cells, the medium was removed and substrates were washed and let dry in the biological cabinet for a couple of hours. Cells of 4×10^4 were seeded onto each sterilized scaffold and allowed to passively infiltrate the scaffolds for 9 d in a cell incubator. Every 3 d cell medium was replaced by fresh medium. After the incubation period, the constructs were processed for cell distribution or SEM analysis. To investigate possible cytotoxic effects due to the IP-DIP resist used to fabricate the scaffold, cell viability and proliferation were investigated using the Trypan blue exclusion test and the bromodeoxyuridine (BrdU) labeling assay, on cells cultured on flat IP-DIP polymerized substrates as previously described [31].

2.5. SEM analysis

Constructs were fixed with 1% Glutaraldehyde (Cat. Number 16210, Electron Microscopy Sciences) in 0.1 M sodium cacodylate solution (NaCaco) (Cat. Number 12300, Electron Microscopy Sciences) for 25 min and post-fixed with 1% osmium tetroxide (Cat. Number 19170, Electron Microscopy Sciences) in NaCaco. Then, samples were dehydrated in a graded series of ethanol (from 25% to 100%) and dried in hexamethyldisilazane (HMDS) (Cat. Number 52619, Sigma-Aldrich), mounted on aluminum stubs and gold (5 nm thick) was sputtered on the samples.

3. Results and discussion

A number of reports have addressed the production of TEVGs and their implementation into clinical trials.

These studies mainly refers to large and medium-size vessels, from 2 to 15 mm diameter [4], obtained either through de-cellularized natural tissues or synthetically constructed [32]. However, arterioles of 50–500 μm diameter have not yet been realized, as such offering a relevant challenge in tissue engineering. In particular, elasto/plastic constraints become a bottleneck of the structure design when attempting to downscale vessel dimensions.

3.1. 3D scaffold structure design and mechanical properties simulation

To design an ideal synthetic vessel analogous, aiming at an average diameter of about 100 microns, we took advantage of FEA mechanical simulations of the CAD software, testing different structure designs for the ability to counteract pressure pulses, a cardinal feature of natural blood vessels and, in particular of small vessels (resistance arterioles). Specifically, we initially carried out simulations on honeycomb, rhombohedral and the squared lower symmetry grid textures; indeed, these textures could be designed using 2PPL using proprietary resist, IP-DIP. Taking also into account in our simulations the physical properties of this polymer, we found that the honeycomb structure redistributed the load in all directions, as required to counteract pressure pulses (data not shown).

The regular hexagonal structure (figure 1(a)) was repeated along a circular symmetry to obtain the conduit, and in a size scalable manner. The geometric parameters d_1 and d_2, that define the scaffold surface porosity, and d_3 (sidewall depth) are showed in figure 1(b). The project design of the cylindrical hollow scaffolds is reported in figure 1(c). We then reasoned that the regular net meshed side structures have to be replicated by the 2PLL. For this, we assumed that the length scales of d_1 and d_2 are practically defined considering the minimal voxel thickness realizable by 2PLL, the typical targeted cell size, and requiring a specific porosity for the cell adhesion. Therefore, d_1 and d_2 were fixed at 3 and 1 μm respectively, while the real-free tuning parameter that can be optimized in this simple high symmetric geometry is d_3, that we optimized by evaluating its effects on the mechanical properties of the honeywell structures. Then, we fine-tailored the cylindrical hollow design maximizing the homogeneity of the elastic response along a free-standing scaffold surface, investigating the application of different homogeneous force fields: in one case, we pushed or stretched the scaffold along the longitudinal Z-axis applying homogeneous force fields to the bases, as shown in figure 2(a), in the other we compressed the scaffold with groups of forces laying on the XY transversal plane, pushing toward the center and maintaining the radial symmetry, as shown in figure 2(e). We also considered the case of localized tangential forces applied at the ends of the scaffold to mimic torsional action on the structure, shown in figure 2(i).

Our FEA simulations allowed us to determine lateral, longitudinal, torsional responses to applied force fields, estimating point by point the relative displacement to the rest condition, aside from the corresponding von Mises stress, as shown in figures 2(c)–(m).

Therefore, to optimize the wall depth d_3, we produced series of simulations for different values of d_3 (wall depths 0.6 μm, 1.2 μm, 2.4 μm, and 5.0 μm) and applied force fields (lateral, longitudinal and torsional loads in table 1). As for the lateral loading, a value of 0.1 MPa have been initially used, calculated from the maximal expected blood pressure (around 100–120 mmHg, i.e. 14–16 kPa) and the lateral effective surface area of the scaffold (about 20% respect to a plain surface). This load is about 60–80 kPa and was furtherly increased to 0.1 MPa to improve the design safety. Then, longitudinal and torsional simulations were performed choosing a load able to produce wide ranges of deformations, from the plastic to elastic regime, observed in the thinner or thicker scaffolds respectively (columns 1–4 table 1).

Table 1 resumes numerically the FEA simulations and the elastic-plastic behavior of the scaffold under different loading conditions. From the Table, only the simulations with $d_3 = 5$ μm give an elastic response of the scaffold, for all the three types of loading. Therefore, a value of $d_3 = 5$ μm was selected for the scaffold design, since only for this condition the safety factor is >1. Besides, with this sidewall depth value, the structure can sustain an increase of the lateral load up to 10 times, maintaining the scaffold deformation in an elastic regime (column 5 and 6 case 1 in table 1). Conversely, longitudinal and torsional loads increases have a more severe effect on the structure deformation, as can be seen from columns 5–7 cases 2 and 3.

It is worth discussing two aspects of this fabrication design. One is that a potential caveat of the above analyses is that we did not directly simulate blood flow with our software, and this remains an issue open for future investigations; that said, we think it is reasonable to postulate, that the material response to a liquid flow should be comparable, at least in first approximation, to repeated applications of traction and compression stresses, as we did here.

A second point of discussion relates to the use of IP-DIP. We chose this material because of its refractive index value that matches with focusing optics (1.52@780 nm); in this way, the resist serves as immersion and photosensitive medium at the same time. By dip-in two-photon laser writing mode, we therefore were able to fabricate 3D structures which height is not limited by objective working distance and substrate thickness. No power compensation was needed, as it typically happens in the case of Nanoscribe or other inverted microscope configurations. As detailed below, IP-DIP also

Table 1. FEA results. Values of the mechanical parameters (principal stresses, displacement, equivalent strain, safety factor) upon the application of different homogeneous force fields on a freestanding scaffold for four different wall depths ($d3 = 0.6, 1.2, 2.4, 5.0$ µm) of the scaffold (reported in the design of figure 1(b)) The equivalent strain is a unitless parameter obtained as Δlength/length units. Color code scale indicates the regimes (from elastic, green, to plastic, orange) deriving from the different combinations of loads and wall depth.

(Case 1) Lateral load	0.1 MPa				0.3 MPa	1 MPa	4 MPa
Wall depth (d_3) (µm)	**0.6**	**1.2**	**2.4**	**5.0**	**5.0**	**5.0**	**5.0**
Von Mises stress (MPa)	0.2 ÷ 54	0.12 ÷ 2.5	0.1 ÷ 1.4	0.005 ÷ 1.2	0.05 ÷ 2.8	0.05 ÷ 37	0.15 ÷ 116
1st principal stress (MPa)	−31 ÷ 45	−3.2 ÷ 3.5	−2.8 ÷ 1.5	−1.6 ÷ 1.1	−2.7 ÷ 3	−28 ÷ 20	−70 ÷ 55
Equivalent strain (%)	<4.3	<1.75	<0.1	<0.08	0 ÷ 0.22	0.01 ÷ 1.5	<9
Safety factor (unit less)	0.7 ÷ 13	>15	>15	>15	>14	1.4 ÷ 13	0.35 ÷ 19
(Case 2) Longitudinal load	**5 mN/point (100 points)**				**10 mN**	**20 mN**	**50 mN**
Wall depth (d_3) (µm)	**0.6**	**1.2**	**2.4**	**5.0**	**5.0**	**5.0**	**5.0**
Von Mises stress (MPa)	14 ÷ 275	23 ÷ 110	7.4 ÷ 64	2.3 ÷ 41	5.2 ÷ 75	7 ÷ 165	20 ÷ 520
1st principal stress (MPa)	−118 ÷ 86	−60 ÷ 100	−42 ÷ 56	−48 ÷ 74	−85 ÷ 110	−170 ÷ 165	−400 ÷ 350
Equivalent strain (%)	0.1 ÷ 12	1 ÷ 5	0.4 ÷ 3	0.1 ÷ 1.4	0.2 ÷ 3.5	0.3 ÷ 10	1 ÷ 26
Safety factor (unit less)	<0.1	0.4 ÷ 2.4	0.8 ÷ 6	1.5 ÷ 9	0.4 ÷ 6	0.2 ÷ 3.1	0.08 ÷ 0.5
(Case 3) Torsional load	**1 mN/point (20 points)**				**2 mN**	**3 mN**	**10 mN**
Wall depth (d_3) (µm)	**0.6**	**1.2**	**2.4**	**5.0**	**5.0**	**5.0**	**5.0**
Von Mises stress (MPa)	16 ÷ 4600	1.3 ÷ 128	0.6 ÷ 73	0.2 ÷ 31	1 ÷ 284	1 ÷ 910	4 ÷ 2300
1st principal stress (MPa)	−1922 ÷ 3634	−96 ÷ 162	−75 ÷ 95	−40 ÷ 48	−190 ÷ 260	−550 ÷ 710	−1300 ÷ 910
Equivalent strain (%)	1 ÷ 320	0.5 ÷ 10	0.2 ÷ 5	<2	<13	<22	0 ÷ 26
Safety factor (unit less)	<0.03	0.19 ÷ 9	0.4 ÷ 12	1 ÷ 23	0.15 ÷ 9	0.04 ÷ 6.2	0.01 ÷ 1.4

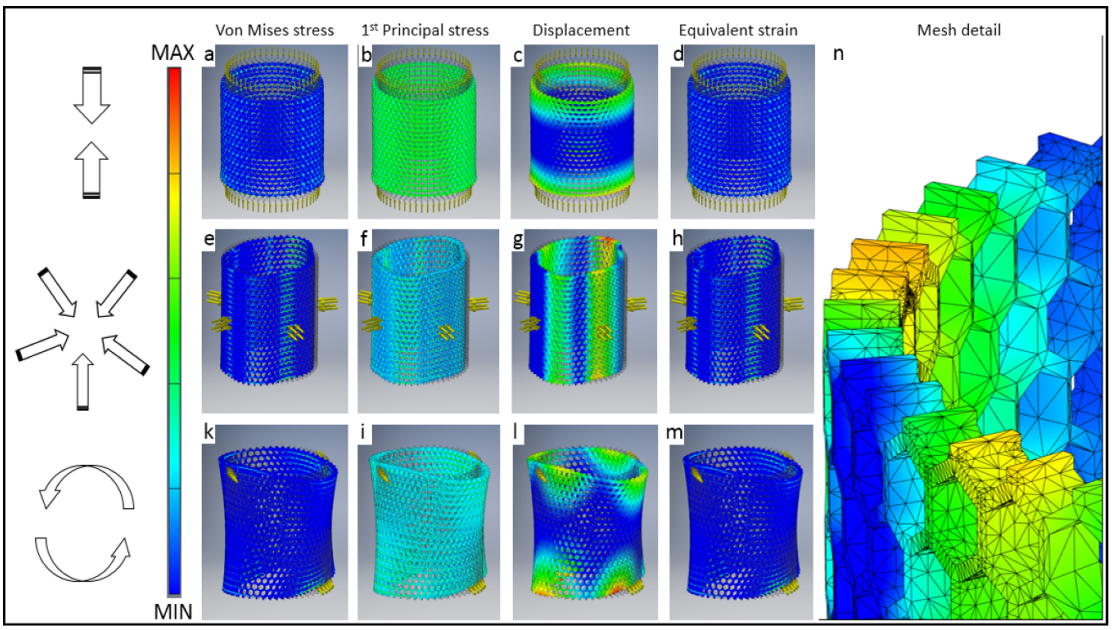

Figure 2. Visual representation of the elastic FEA results for the 2PLL IP-dip scaffold shown in figure 1, stressed by three different force configurations indicated aside as explained in 2.1 and 3.1. For simulations, we considered respectively top and bottom homogeneously distributed forces of 250 + 250 mN, lateral pressure along with five stripes at 100 KPa intensity, and two torsional force couples of 10 + 10 mN applied at the terminus coronas of the scaffold. In the figure are shown the visual description of the von Mises stress distribution for the overall component, panels (a), (e) and (k), the first principal stress, figures (b), (f) and (i), the local displacement figures (c), (g), (l), and the equivalent strain in figures (d), (h), (m) of the scaffold under three different exemplifying load conditions as described in paragraph 2.1. Figure (n), detail of (l), highlights the adaptive mesh used. The visual color scale allows the direct evaluation of regions of high stress and in between the safety factor range. 1st principal stress gives the value of stress that is normal to the plane in which the shear stress is zero helping to understand the maximum tensile stress induced in the solid due to the loading conditions. Differently, the equivalent strain is a unitless quantity obtained as Δ_{length}/length units.

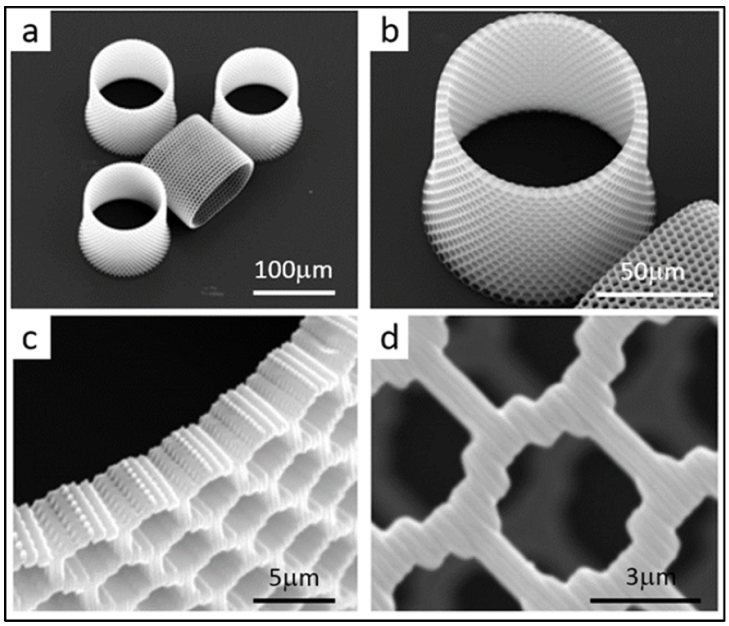

Figure 3. Low-magnification (a), (b) and high-magnification (c), (d) SEM images collected from an array of 3D scaffolds fabricated by 2PLL to produce the controlled porous architecture with the designed dimensions ($d_1 = 3$ µm, $d_2 = 1$ µm, $d_3 = 5$ µm). Reported structure details (c), (d) show the surface texture produced during 2PLL fabrication, determined by the voxel movement during the additive building process.

allowed fast fabrication. The use of other polymers is certainly possible and might allow to expand the properties and performances of these microvessels. It is tempting to speculate, for example, the use of biodegradable polymers amenable to 2PLL for both chemical crosslinking and optical properties, such as PLA [20], or soft hydrogels [33–36]. The mechanical properties of PLA or hydrogels are similar

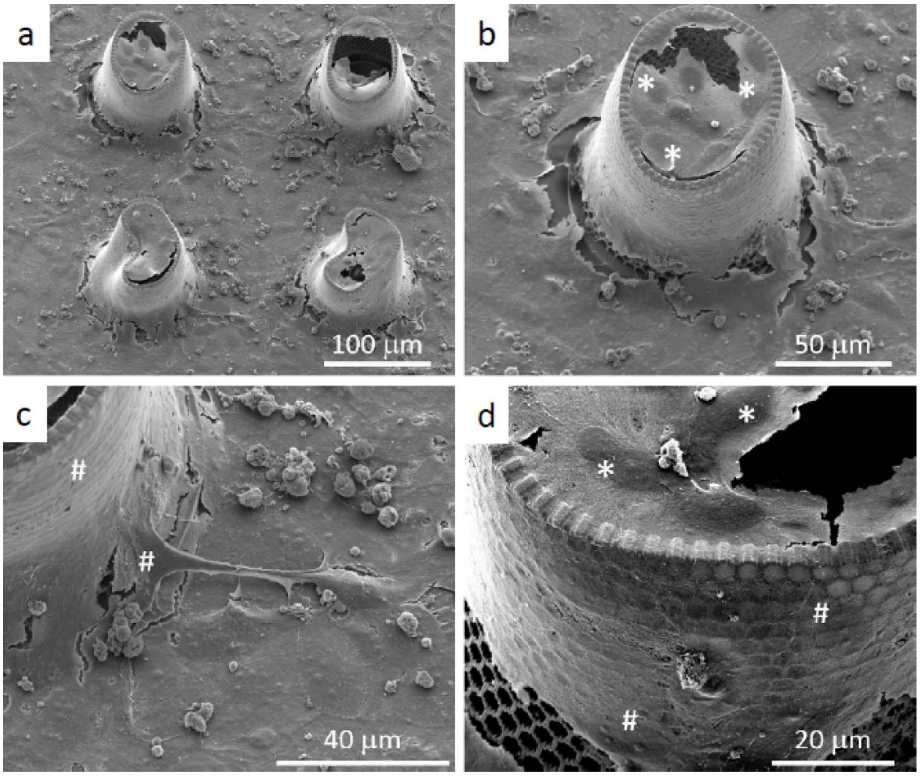

Figure 4. Representative low-magnification (a), (b) and high-magnification (c), (d) SEM images of 9 d *in vitro* cultures of HUVECs on TEVG.

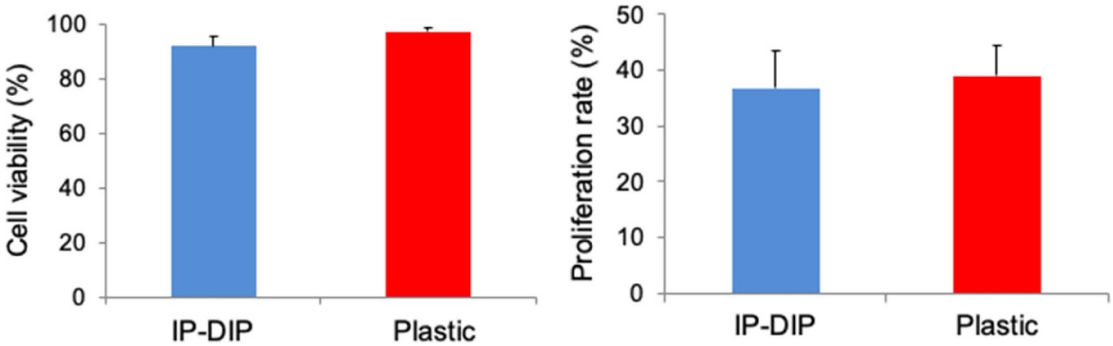

Figure 5. Trypan blue exclusion test assessing cells viability (left) and the bromodeoxyuridine (BrdU) labeling assay of proliferation (right).

to IP-DIP or closer to those of natural tissues, respectively. However, the simulation results here described can be fully exploited only for polymers that have similar bulk mechanical properties of IP-DIP, while soft hydrogels might require ad hoc exploitation of distinct bioengineering protocols.

3.2. 3D-shaped porous scaffolds

Next, we aimed to fabricate the simulated scaffold of figure 1(c) by the 2PLL computer aided manufacturing, CAM. The choice to microfabricate the scaffolds via the 2PLL-CAM technique was selected because it offered the possibility to scale down the size of the vessel nearly arbitrarily. Indeed, the ultimate resolution obtainable with such technique, is down to the sub-micron scale, as already reported [37, 38], enabling us to fabricate the designed features (dimensions from 1 to 5 µm) with high accuracy. Figure 3 shows SEM images of an array of tubular structures fabricated by 2PLL. One tubular scaffold detached from the substrate (figures 3(a) and (b)) allowed an easy inspection of the structure, and showed an overall height of 80 ± 1 µm, resulting in a maximum 20% shrinkage in the scaffold' axial direction. The smallest lateral feature size of the structure was 0.9 µm (figure 3(d)), demonstrating a 10% shrinkage in the tangential direction. The grid pattern was still regular with a periodic z-pitch of 8 µm, without any significant distortion. The wall thickness of each tube was 5 µm, suggesting negligible thickness shrinkage in the radial direction. The two-photon direct laser writing

process was performed in an additive scheme with a 0.6 μm slicing distance and 0.3 μm hatching distance. As such, the scaffold surface texture was evident from surface details shown in figures 3(c) and (d). The tubular shape structure took the minimum fabrication time for approximately 10 min, using scanning speeds of 8–10 mm s^{-1}, which is a two-photon polymerization, 2PP, high-speed. In fact, in our setup, the applied x–y galvanometric mirror scanners provide very stable laser scanning in the liquid photosensitive material during the 2PP structuring, resulting in the realization of highly accurate, fast 2PP processing up to the mesoscale.

3.3. Cell cultures

Few results are reported on 2PLL microfabrication of porous scaffolds using proprietary Nanoscribe resists on which cell culturing allow to guide different behavior of tissue specific cell [39]. Examples are neuronal networks formation [40], iPSC-derived retinal cells [41] migration of human dendritic cells [42]. Here we asked if the fabricated scaffold can sustain endothelial cells adhesion and proliferation. For this, HUVEC endothelial cells were seeded on petri dishes containing the fabricated scaffolds. Nine days post-seeding samples were analyzed by SEM. As shown in figure 4, HUVECs adhered to the scaffold surface during this time. Cells, initially attaching sparsely to the substrate, were able to proliferate by forming a continuous confluent external monolayer on the micro-designed tube. Part of the seeded cells covered the hole on the top of the ring (white asterisk, figures 4(b) and (d)) not filtering inside, while a large portion attached and growth on the sidewall of the capillary (white crosshatch, figures 4(c) and (d)). Cell Hoechst 33342 DNA assay gave us indications regarding the number of cells that attached to the scaffold and growth. Normal nuclei were visible in HUVEC cells with no morphological alterations or chromatin condensation, typical of apoptotic cells. To investigate cellular viability and proliferative fitness on the substrate here used for fabrication, we carried out trypan blue exclusion assays and BrDU labeling, respectively, on cells cultured on flat IP-DIP surfaces. As shown in figure 5, no ostensible difference could be detected in the viability and proliferative capacity of cells attached to IP-DIP compared to standard tissue culture plastics [43].

4. Conclusions

3D micro-vessels analogues were designed and fabricated by 2PLL, using synthetic photoresist, IP-DIP Nanoscribe photoresist, that has already been demonstrated to be biocompatible and supporting cell adhesion [39–43] and does not undergo to relevant hydrolytic degradation during permanence in cell medium. The geometrical scaffold fabrication parameters were obtained on the base of FEA of mechanical simulation, to realize porous scaffolds that can sustain large elastic forces. Thanks to the intrinsic high resolution of 3D two photons fabrication technique, a hundred micron diameter cylindrical hollow scaffold with an ad hoc honeycomb fine wall surface texture has been created, with wall thickness of 5 μm and hexagonal cell length and thickness of 3 and 1 μm respectively, thus allowing to control in detail the architecture, porosity, and shape of the scaffold. Our preliminary *in vitro* studies have not demonstrated any relevant toxic effects exhibited by the scaffold on HUVEC cells, supporting their adhesion and growth, offering new opportunities in regenerative medicine. A challenge for the future development of these results may be the use of a biodegradable material, specially designed for 2PP but that is progressively able to degrade allowing natural tissue regeneration, as well as to release of growth factors or pharmaceutical media.

Acknowledgments

G B acknowledges the University of Padova for financial support of through 'Finanziamento per le attrezzature scientifiche finalizzate alla ricerca—Bando 2013' and SID project '3D Engineered Biopolymers Micro Fabrication by Two-Photon Laser Additive Manufacturing'. A G acknowledges financial support from the King Abdullah University of Science and Technology (KAUST) Universita' degli Studi di Padova funding through CRG5 project OSR award #: OCRF-2016-CRG5.

ORCID iDs

T Limongi https://orcid.org/0000-0001-5510-5561
L Brigo https://orcid.org/0000-0001-6703-3921
L Tirinato https://orcid.org/0000-0001-9826-2129
F Pagliari https://orcid.org/0000-0002-5547-222X
A Giugni https://orcid.org/0000-0003-2845-9828
G Brusatin https://orcid.org/0000-0002-5219-8376

References

[1] Roth G A *et al* 2017 Global, regional, and national burden of cardiovascular diseases for 10 causes, 1990–2015 *J. Am. Coll. Cardiol.* **70** 1–25
[2] Kim K-W, Won Y L, Ko K S, Heo K-H and Chung Y H 2012 The effects of hazardous chemical exposure on cardiovascular disease in chemical products manufacturing workers *Toxicol. Res.* **28** 269–77
[3] McPherson R and Tybjaerg-Hansen A 2016 Genetics of coronary artery disease *Circ. Res.* **118** 564–78
[4] Pashneh-Tala S, MacNeil S and Claeyssens F 2016 The tissue-engineered vascular graft—past, present, and future *Tissue Eng. Part B Rev.* **22** 68–100
[5] Limongi T, Tirinato L, Pagliari F, Giugni A, Allione M, Perozziello G, Candeloro P and Di Fabrizio E 2017

Fabrication and applications of micro/nanostructured devices for tissue engineering *Nanomicro Lett.* **9** 1
[6] Limongi T *et al* 2017 Laboratory injection molder for the fabrication of polymeric porous poly-epsilon-caprolactone scaffolds for preliminary mesenchymal stem cells tissue engineering applications *Microelectron. Eng.* **175** 12–6
[7] Kurobe H, Maxfield M W, Breuer C K and Shinoka T 2012 Concise review: tissue-engineered vascular grafts for cardiac surgery: past, present, and future *Stem Cells Transl. Med.* **1** 566–71
[8] Fischer J, Von freymann G and Wegener M 2010 The materials challenge in diffraction-unlimited direct-laser-writing optical lithography *Adv. Mater.* **22** 3578–82
[9] Barner-Kowollik C, Bastmeyer M, Blasco E, Delaittre G, Müller P, Richter B and Wegener M 2017 3D laser micro- and nanoprinting: challenges for chemistry *Angew. Chem., Int. Ed.* **56** 15828–45
[10] Ibrahim S, Higgins D A and Ito T 2007 Direct-write multiphoton photolithography: a systematic study of the etching behaviors in various commercial polymers *Langmuir* **23** 12406–12
[11] Teh W H, Dürig U, Drechsler U, Smith C G and Güntherodt H-J 2005 Effect of low numerical-aperture femtosecond two-photon absorption on (SU-8) resist for ultrahigh-aspect-ratio microstereolithography *J. Appl. Phys.* **97** 054907
[12] Koskela J E, Turunen S, Ylä-Outinen L, Narkilahti S and Kellomäki M 2012 Two-photon microfabrication of poly(ethylene glycol) diacrylate and a novel biodegradable photopolymer-comparison of processability for biomedical applications *Polym. Adv. Technol.* **23** 992–1001
[13] Matsuzaki Y, John K, Shoji T and Shinoka T 2019 The evolution of tissue engineered vascular graft technologies: from preclinical trials to advancing patient care *Appl. Sci.* **9** 1274
[14] Chen C-W, Corselli M, Péault B and Huard J 2012 Human blood-vessel-derived stem cells for tissue repair and regeneration *J. Biomed. Biotechnol.* **1–9** 2012
[15] Wilcox J N and Scott N A 1996 Potential role of the adventitia in arteritis and atherosclerosis *Int. J. Cardiol.* **54** S21–35
[16] Nemeno-Guanzon J G, Lee S, Berg J R, Jo Y H, Yeo J E, Nam B M, Koh Y-G and Lee J I 2012 Trends in tissue engineering for blood vessels *J. Biomed. Biotechnol.* **2012** 1–14
[17] Sears N A, Seshadri D R, Dhavalikar P S and Cosgriff-Hernandez E 2016 A review of three-dimensional printing in tissue engineering *Tissue Eng. Part B Rev.* **22** 298–310
[18] Lee J W 2015 3D nanoprinting technologies for tissue engineering applications *J. Nanomater.* **2015** 1–14
[19] Lee S-H, Moon J J and West J L 2008 Three-dimensional micropatterning of bioactive hydrogels via two-photon laser scanning photolithography for guided 3D cell migration *Biomaterials* **29** 2962–8
[20] Koroleva A, Gill A A, Ortega I, Haycock J W, Schlie S, Gittard S D, Chichkov B N and Claeyssens F 2012 Two-photon polymerization-generated and micromolding-replicated 3D scaffolds for peripheral neural tissue engineering applications *Biofabrication* **4** 025005
[21] Kufelt O, El-Tamer A, Sehring C, Meißner M, Schlie-Wolter S and Chichkov B N 2015 Water-soluble photopolymerizable chitosan hydrogels for biofabrication via two-photon polymerization *Acta Biomater.* **18** 186–95
[22] Elomaa L and Yang Y P 2017 Additive manufacturing of vascular grafts and vascularized tissue constructs *Tissue Eng. Part B Rev.* **23** 436–50
[23] Ong C S, Zhou X, Huang C Y, Fukunishi T, Zhang H and Hibino N 2017 Tissue engineered vascular grafts: current state of the field *Expert Rev. Med. Devices* **14** 383–92
[24] Best C, Strouse R, Hor K, Pepper V, Tipton A, Kelly J, Shinoka T and Breuer C 2018 Toward a patient-specific tissue engineered vascular graft *J. Tissue Eng.* **9** 204173141876470
[25] Greiner A M, Richter B and Bastmeyer M 2012 Micro-engineered 3D scaffolds for cell culture studies *Macromol. Biosci.* **12** 1301–14
[26] Spagnolo B, Brunetti V, Leménager G, De Luca E, Sileo L, Pellegrino T, Paolo Pompa P, De Vittorio M and Pisanello F 2015 Three-dimensional cage-like microscaffolds for cell invasion studies *Sci. Rep.* **5** 10531
[27] Marino A, Barsotti J, de Vito G, Filippeschi C, Mazzolai B, Piazza V, Labardi M, Mattoli V and Ciofani G 2015 Two-photon lithography of 3D nanocomposite piezoelectric scaffolds for cell stimulation *ACS Appl. Mater. Interfaces* **7** 25574–9
[28] Bauer J, Hengsbach S, Tesari I, Schwaiger R and Kraft O 2014 High-strength cellular ceramic composites with 3D microarchitecture *Proc. Natl Acad. Sci.* **111** 2453–8
[29] Bauer J, Schroer A, Schwaiger R and Kraft O 2016 Approaching theoretical strength in glassy carbon nanolattices *Nat. Mater.* **15** 438–43
[30] Meza L R, Zelhofer A J, Clarke N, Mateos A J, Kochmann D M and Greer J R 2015 Resilient 3D hierarchical architected metamaterials *Proc. Natl Acad. Sci.* **112** 11502–7
[31] Dupont S *et al* 2011 Role of YAP/TAZ in mechanotransduction *Nature* **474** 179–85
[32] Qu J, Kadic M, Naber A and Wegener M 2017 Micro-structured two-component 3D metamaterials with negative thermal-expansion coefficient from positive constituents *Sci. Rep.* **7** 40643
[33] Kunwar P, Xiong Z, Zhu Y, Li H, Filip A and Soman P 2019 Hybrid laser printing of 3D, multiscale, multimaterial hydrogel structures *Adv. Opt. Mater.* **7** 1900656
[34] Xiong Z, Li H, Kunwar P, Zhu Y, Ramos R, Mcloughlin S, Winston T, Ma Z and Soman P 2019 Femtosecond laser induced densification within cell-laden hydrogels results in cellular alignment *Biofabrication* **11** 035005
[35] Brigo L, Urciuolo A, Giulitti S, Della Giustina G, Tromayer M, Liska R, Elvassore N and Brusatin G 2017 3D high-resolution two-photon crosslinked hydrogel structures for biological studies *Acta Biomater.* **55** 373–84
[36] Giustina G D, Giulitti S, Brigo L, Zanatta M, Tromayer M, Liska R, Elvassore N and Brusatin G 2017 Hydrogel with orthogonal reactive units: 2D and 3D cross-linking modulation *Macromol. Rapid Commun.* **38** 1–8
[37] Liu Y, Campbell J H, Stein O, Jiang L, Hund J and Lu Y 2018 Deformation behavior of foam laser targets fabricated by two-photon polymerization *Nanomaterials* **8** 498
[38] Brigo L, Maria Schmidt J E, Gandin A, Michieli N, Colombo P and Brusatin G 2018 3D nanofabrication of SiOC ceramic structures *Adv. Sci.* **5** 1800937
[39] Kim S, Lee S and Choi H 2016 Review on fabrication and manipulation of scaffold and ciliary microrobots *Hanyang Med. Rev.* **36** 235
[40] Fendler C, Denker C, Harberts J, Bayat P, Zierold R, Loers G, Münzenberg M and Blick R H 2019 Microscaffolds by direct laser writing for neurite guidance leading to tailor-made neuronal networks *Adv. Biosyst.* **3** 1800329
[41] Worthington K S, Wiley L A, Kaalberg E E, Collins M M, Mullins R F, Stone E M and Tucker B A 2017 Two-photon polymerization for production of human iPSC-derived retinal cell grafts *Acta Biomater.* **55** 385–95
[42] Holm Olsen M, Hjortø G M, Hansen M, Met Ö, Svanebc I M and Larsen N B 2013 In-chip fabrication of free-form 3D constructs for directed cell migration analysis *Lab Chip* **13** 4800–9
[43] Milcovich G, Contessotto P, Marsico G, Ismail S and Pandit A 2017 Synthetic/ECM-inspired hybrid platform for hollow microcarriers with ROS-triggered nanoporation hallmarks *Sci. Rep.* **7** 13138